Catalysis Science & Technology

Accepted Manuscript

ROYAL SOCIETY OF CHEMISTRY

www.rsc.org/catalysis

ARTICLE

Influence of nickel content on structural and surface properties, reducibility, and catalytic behavior of mesoporous γ-alumina-supported Ni–Mg oxides for pre-reforming of liquefied petroleum gas

Received 00th January 20xx,
Accepted 00th January 20xx

DOI: 10.1039/x0xx00000x

www.rsc.org/

Mingwu Tan, Xueguang Wang*, Yong Hu, Xingfu Shang, Li Zhang, Xiujing Zou, Weizhong Ding and Xionggang Lu*

Mesoporous γ-alumina-supported Ni–Mg oxides (*x*NiO–MgO/γ-MA) with various mass percentage contents of nickel (*x* = 0, 5, 10, 15, 18, and 21) were prepared through one-pot hydrolysis of metal nitrate salts without surfactants. Influences of nickel content on catalyst structure, surface properties, interaction between Ni species and support, reducibility of Ni^{2+} ions, and Ni particle dispersion were investigated in detail using XRD, N_2 sorption, TEM, XPS, CO_2-TPD, H_2-TPR, hydrogen chemisorption, and TG techniques. The *x*NiO–MgO/γ-MA materials showed wormhole-like mesoporous structures with large surface areas and narrow pore size distributions. The dominant NiO species were homogeneously dispersed with an attenuated interaction by the support with the increase in Ni content, producing uniform Ni nanoparticles throughout γ-alumina frameworks after H_2 reduction. The Ni particle sizes decreased with increasing Ni content and showed a minimum at 18 wt %, likely due to Ni crystallite growth by Ostwald ripening rather than by migration of Ni nanoparticles. The reduced *x*Ni–MgO/γ-MA catalysts were investigated for catalytic behaviors in pre-reforming of liquefied petroleum gas. The results demonstrated that Ni surface areas were mainly responsible for catalytic activities; smaller Ni nanoparticles benefited steam reforming of hydrocarbons, methanation of carbon oxides, and water gas shift, but inhibited hydrocracking of hydrocarbons and lowered rate of coke deposition, improving catalytic activity and stability.

1. Introduction

Hydrogen has attracted considerable attention as a promising energy carrier for potential stationary and mobile applications because of the high intrinsic energy efficiency of fuel cells.[1–3] There are several different catalytic approaches for hydrogen production from natural gas and various liquid fuels, including carbon dioxide reforming,[4] partial oxidation reforming,[5] steam reforming,[6] and auto-thermal reforming.[7] Catalytic steam reforming of liquid fuels has been recognized as a feasible process for hydrogen production for compact and efficient polymer electrolyte membrane fuel cells (PEMFCs) because this type of reforming produces the highest quantity of hydrogen in the product stream and eliminates the needs for air compressor and related component units.[8,9] Compared to natural gas, liquid higher hydrocarbons such as liquefied petroleum gas (LPG) is believed to be a preferred feedstock for low-cost distributed hydrogen production due to their higher energy density, easy storage and transportation, and well-established existing infrastructures.[10–15] However, the steam reforming of higher hydrocarbons is more prone to produce coke deposition from thermal cracking of hydrocarbons at high temperatures, causing significant catalyst deactivation and reactor plugging.[16–18] Thus, low-temperature steam reforming (or pre-reforming) was developed not only to increase fuel saving, but also to reduce thermal decomposition of fuel.[19–21]

Alumina-supported nickel catalysts have widely been investigated for steam reforming of hydrocarbons due to their high intrinsic catalytic activity and low cost. However, conventional alumina-supported nickel catalysts have the prime drawback of rapid deactivation, which is derived from coke deposition, nickel particle sintering, and phase transformation in the reforming processes.[22–25] It is well known that chemical composition and preparation procedure of supported nickel catalysts significantly influence the catalyst structure, surface properties, reducibility and sintering of nickel oxide species, and the dispersion of nickel particles, resulting in substantial changes in the catalytic properties. Thus, considerable efforts are being undertaken to improve resistance to coke deposition and to prevent nickel particle sintering through adding structural and electronic promoters, modifying surface properties of support, improving preparation routes, and carefully adjusting catalyst composition, etc.[26–36]

A majority of alumina-supported Ni catalysts have been prepared by wet impregnation method, and many studies have been devoted to fundamental aspects.[37–43] However, the

[a] State Key Laboratory of Advanced Special Steel, Shanghai University, Shanghai 200072, China. E-mail: wxg228@shu.edu.cn (X. G. Wang); luxg@shu.edu.cn (X. G. Lu).

understanding of interrelations among the active Ni species, the catalyst structure and surface characteristics, and the catalytic properties in the reforming reactions is still ambiguous, due to the inherently inhomogeneous metal dispersion and porous structure.

Recently, we have successfully synthesized mesoporous γ-alumina (γ-MA)-supported Ni and Ni–Mg mixed oxides with large surface areas, pore volumes and narrow pore size distributions through one-pot partial hydrolysis of nitrate salts.[44–46] Ni–Mg oxide species were homogeneously distributed in γ-MA frameworks and produced uniformly dispersed Ni nanoparticles after H_2 reduction. The reduced γ-MA-supported Ni–MgO catalysts showed much higher stability and coke resistance ability for the pre-reforming of LPG than either the ordered mesoporous alumina-supported Ni–MgO catalyst with amorphous framework walls obtained via the one-pot surfactant-assisted strategy[34,47] or γ-MA-supported Ni–MgO catalyst via the traditional impregnation route.[45] Our previous studies have detailedly analyzed the influences of the preparation method, calcination temperature and MgO promoter on the physical and chemical properties and the catalytic properties of γ-MA-supported Ni–MgO catalysts for pre-reforming of LPG.

It has been reported that content of active Ni is intimately related to the reducibility of Ni species and the sizes and surface areas of Ni particles, which determine the catalytic activity, stability, and resistance to coke deposition in the steam reforming.[29,48,49] In this work, mesoporous γ-alumina-supported Ni–Mg oxide materials with various Ni contents were prepared through the one-pot hydrolysis. Influences of Ni content on structural and surface properties, reducibility of Ni^{2+} ions, sizes and surface areas of Ni particles, and catalytic properties for pre-reforming of LPG were discussed in detail.

2. Experimental section

2.1. Preparation of γ-MA-supported Ni–Mg catalysts

Analytical-grade $Al(NO_3)_3{\cdot}9H_2O$, $Mg(NO_3)_2{\cdot}6H_2O$, $Ni(NO_3)_2{\cdot}6H_2O$ and $(NH_4)_2CO_3$ were purchased from Sinopharm Chemical Reagent Co., Ltd., and used as received.

The γ-MA-supported Ni–Mg oxide catalysts were prepared through the one-pot hydrolysis of nitrate salts.[45,46] 0.1 mol of $Al(NO_3)_3{\cdot}9H_2O$ and 0.025 mol of $Mg(NO_3)_2{\cdot}6H_2O$ along with required amounts of $Ni(NO_3)_2{\cdot}6H_2O$ were dissolved in 50 mL of deionized water and heated to 70 °C. 1 mol L^{-1} $(NH_4)_2CO_3$ aqueous solution was slowly added (0.9 mL min^{-1}) into the above solution with vigorous stirring until a sudden formation of monolithic green and transparent gel appeared. After aged at 30 °C for 48 h, the crude gel was dispersed in an open glass dish at 100 °C for 24 h, and followed by treating in two steps at 150 °C and 200 °C in air in a muffle furnace in the hood for 10 h, respectively, to remove ammonium nitrate. Finally, the treated solid was calcined in air at 400 °C for 10 h at a heating rate of 1 °C min^{-1}. The previous investigations indicated that γ-MA-supported Ni–Mg catalysts with the nominal Mg/Al molar ratio of 0.25 calcined at 400 °C and reduced at 600 °C, had the optimum catalytic performance for the pre-reforming of LPG.[45,46] Therefore, in the present study, the nominal Mg/Al molar ratio was fixed at 0.25, and the calcination and the reduction temperatures of the catalysts used in the activation process were 400 °C and 600 °C, respectively. The resulting γ-MA-supported Ni–Mg oxide materials were designated as *x*NiO–MgO/γ-MA and read as *x*Ni–MgO/γ-MA after H_2 reduction, where *x* represents the nominal Ni content in wt %.

2.2. Catalyst characterization

The powder X-ray diffraction (XRD) patterns of the calcined, reduced and spent catalysts were obtained on a Rigaku D/MAX-2200 diffractometer with a Cu Kα radiation (λ = 0.15418 nm) at a voltage of 40 kV and a current of 40 mA. The *x*Ni–MgO/γ-MA samples reduced and spent for the XRD analysis were immediately transferred in N_2 in a sealed container. The crystallite sizes of γ-Al_2O_3 and metal Ni were estimated using the full widths at half maximum (FWHM) of the Al_2O_3 (4 4 0) and Ni (2 0 0) peaks, respectively, through the Scherrer equation.[45,46]

Scanning electron microscopy (SEM) images were obtained using a Hitachi S-4800 electron microscope. TEM micrographs were performed with a JEOL JEM-2010F microscope operating at 200 kV. The sample was prepared by placing a drop of ethanol solution of catalyst powder onto a carbon-coated copper grid. Size distributions of Ni particles were determined by counting ca. 200–250 particles in TEM images.

N_2 adsorption and desorption measurements were carried using a Micromeritics ASAP 2020 Sorptometer at liquid nitrogen temperature (–196 °C). The samples were degassed at 300 °C for at least 6 h. The specific surface area (S_{BET}) was calculated using the Brunauer–Emmett–Teller (BET) method. The pore size distribution curve was calculated using the desorption branch of the isotherms and the Barrett–Joyner–Halenda (BJH) method. The pore size (Dp) was obtained from the peak maximum of the distribution curve, and the average pore size (Da) was calculated from all pores of various sizes by the BJH method. The pore volume (Vp) was estimated from the adsorbed amount at the P/P_0 = 0.990 single point.

X-ray photoelectron spectra (XPS) were measured on an ESCALAB 250Xi spectrometer. This spectrometer used an aluminum anode (Al Kα = 1486.6 eV) operated at 12 kV and 20 mA. The instrument was performed at a pressure of ca. 1×10^{-9} Torr. The catalyst powder was placed on a sample holder and pressed into self-supported wafer. Binding energies were measured with a precision of ± 0.2 eV or better. The spectra for the samples were calibrated using the binding energy of Al 2p peak at 73.8 eV with respect to γ-Al_2O_3 support.

CO_2 temperature-programmed desorption (CO_2-TPD) was carried out on a Micromeritics ASAP 2920 Sorptometer to analyze the surface basic properties of the catalysts. For the *x*NiO–MgO/γ-MA sample, 100 mg of sample was pretreated in a He flow (30 mL min^{-1}) at 300 °C for 0.5 h and then cooled to 50 °C and exposed to 10 vol % CO_2/He atmosphere (30 mL/min) for 1 h. After this, the sample was purged with a He flow (30 mL min^{-1}) for 1 h. Finally, CO_2-TPD was performed to 700 °C with a temperature ramp of 10 °C min^{-1}. The amount of

absorbed CO_2 was measured with a gas chromatograph equipped with a thermal conductivity detector (TCD). The CO_2-TPD procedure for the *x*Ni–MgO/γ-MA sample was the same, except that prior to the measurement, the *x*NiO–MgO/γ-MA sample was reduced in situ in a mixed flow of 20 vol % H_2/N_2 (50 mL min^{-1}) at 600 °C for 2 h.

H_2 temperature-programmed reduction (H_2-TPR) was carried out on an apparatus in a conventional flow system with a moisture trap to observe the reducibility of the *x*NiO–MgO/γ-MA catalysts. 100 mg of sample placed in a quartz reactor was first pretreated in an Ar stream (30 mL min^{-1}) at 300 °C for 0.5 h, then cooled to room temperature. H_2-TPR was conducted with a gas mixture of 5 vol % H_2 in Ar at 30 mL min^{-1}. The temperature was raised to 1000 °C at a heating rate of 10 °C min^{-1}. The amount of H_2 uptake was measured with TCD.

The surface area of metal Ni was determined using the Micromeritics ASAP 2020 sorptometer by H_2 chemisorption. 1.5 g *x*NiO–MgO/γ-MA catalyst was placed in a quartz sample cell and treated in a He flow (30 mL min^{-1}) at 100 °C for 1 h. The sample was evacuated and then purged in flowing H_2 for 5 min, and finally reduced in a H_2 flow (50 mL min^{-1}) at 600 °C for 2 h at a heating rate of 10 °C min^{-1}. After this, the sample was evacuated at 400 °C to 10 μmHg to remove the impurities for 30 min and cooled to 45 °C for 5 min for H_2 chemisorption. The method of the double isotherm was used to determine the irreversibly bound chemisorbed H_2, determined by extrapolating the linear part of the isotherm in the range of 95–450 mmHg to zero pressure, which should correspond to H_2 adsorbed on the metallic Ni surface, considering an irreversible adsorption on the surface of the metallic Ni particles and a reversible adsorption on the support surface. The reproducibility of the experiments was performed at least three times with a margin of error of less than 2%. The Ni surface area was calculated by assuming that one hydrogen atom occupies on one surface Ni atom and that the cross-sectional area of the Ni atom is 6.49×10^{-20} m^2.

The amount of carbon deposition on the used samples was determined with a thermogravimetric analyzer (STA 4449 F3). The samples were first heat preserved at 50 °C for 0.5 h and then with a heating speed of 10 °C min^{-1} from 50 °C in an air flow of 30 mL min^{-1} to 800 °C.

2.3. Catalyst test and analysis

The pre-reforming of LPG was performed in the conventional fixed-bed reactor. LPG (purchased from Shanghai Auto Energy Co. Ltd), consisting of C_2H_6 of 3.1 vol %, C_3H_8 of 84.0 vol %, and C_4H_{10} of 12.9 vol %, was used to study the catalytic properties of the *x*Ni–MgO/γ-MA catalysts. A preheater filled with quartz balls with a set temperature of 300 °C was used to vaporize water and fully mix the reaction gases. The reaction gases and water were controlled using the mass flow controllers and a HPLC pump, respectively. The catalyst temperature was monitored using a thermocouple put in the middle of the catalyst bed. Typically, 100 mg of catalyst (40–60 mesh) diluted with 400 mg of quartz particles (40–60 mesh) was placed between two layers of quartz wool in the centre of the reactor for each run. Prior to the reaction, the catalyst was reduced in situ in a mixed flow of 20 vol % H_2/N_2 (50 mL min^{-1}) at a heating rate of 10 °C min^{-1} to 600 °C, maintained for 2 h, and then cooled to 450 °C for 0.5 h. After this, the steam (the amount required in the reaction) was pumped for ca. 5 min to avoid initial carbon deposition, followed by introducing LPG into the reaction system under atmospheric pressure and closing the N_2 and H_2 valves. After the 1-h reaction, the reaction system became stable, and the effluent gas was cooled in a condenser at room temperature and passed a drierite bed to remove all water. Finally, the dried gas products were analyzed using an on-line GC-FID gas chromatograph with a CP–sil 5 CB column for hydrocarbons, followed by another GC-TCD gas chromatograph for CH_4, CO and CO_2, and H_2. The reaction was terminated by closing the LPG and water valves and cooled quickly by keeping the 100 mL min^{-1} N_2 flow and opening the furnace. The flow rate of outlet gas was measured by a soap flow meter. Other than H_2, CO, CO_2, and CH_4, no other products were observed in the exit gas. The overall mass balance was more than 97% on the basis of carbon in the starting reactants.

The conversion of LPG (X_{LPG}) and the selectivity of the carbon-containing product *i* (*i* = CH_4, CO, CO_2) (S_i) and H_2 selectivity (S_{H2}) formed were calculated with the formulae (Eqs. (1)–(3)), where N represents the molar number, and shown as follows:

$$X_{LPG} = \frac{\sum \mathrm{N_i}}{N_{carbon} \text{ in the feed}} \times 100\% \quad (1)$$

$$S_i = \frac{N_i}{\sum N_i} \times 100\% \quad (2)$$

$$S_{H2} = \frac{N_{H2}}{(N_{H2} + 2 \times N_{CH4})} \times 100\% \quad (3)$$

The turnover frequencies (TOFs) of the *x*Ni–MgO/γ-MA catalysts for the pre-reforming of LPG are defined as the number of converted carbon atoms in LPG per surface metal Ni atom and hour. Considering that the reforming reaction of LPG for TOF measurements should be conducted at a low LPG conversion (≤ 20%) without channelling to precisely determine the actual reaction rate on the metal active site, a 25 mg catalyst (60–80 mesh) diluted with 200 mg of quartz particles (60–80 mesh) was used for the reaction, in which the GHSV was fixed at 3.3×10^5 mL g_{cat}^{-1} h^{-1}, unless specified otherwise.

3. Results and discussion

3.1 Physicochemical properties of *x*NiO–MgO/γ-MA materials

3.1.1 XRD characterization

Fig. 1 presents the XRD patterns of the *x*NiO–MgO/γ-MA (*x* = 0, 5, 10, 15, 18, and 21) materials. All the *x*NiO–MgO/γ-MA materials showed three strong diffraction peaks around 2θ = 37°, 45°, and 66°, corresponding to the (3 1 1), (4 0 0), and (4 4 0) planes for γ-Al_2O_3 phase and/or Ni(Mg)Al_2O_4 spinel, respectively. This result indicated that the addition of $Ni(NO_3)_2$ along with $Mg(NO_3)_2$ had hardly effect on the transformation of aluminum hydroxides and oxyhydroxides into γ-Al_2O_3 in the gel precursors at 400 °C, just like those for γ-MA.[44] When

nickel content was less than 18 wt %, no characteristic diffraction peaks associated with MgO and/or NiO phases were observed, which are indiscernible due to the high similarity of the XRD patterns.[50,51] This result demonstrated that Ni oxide species along with Mg oxide species were highly dispersed in the form of amorphous phase or very fine particles below the detection limit of XRD, or interacted with alumina to form $Ni(Mg)Al_2O_4$ spinel in the *x*NiO–MgO/γ-MA matrices.[10,52] With increasing the Ni content to 21 wt %, an additional peak at 2θ = 43.3° occurred, suggesting that free MgO and/or NiO phases or larger oxide crystallites were formed in the matrices.[46]

γ-Al_2O_3 (PDF no. 10–0425), $MgAl_2O_4$ (PDF no. 21–1152) and $NiAl_2O_4$ (PDF no. 10–0339) spinel phases are difficult to be distinguished from each other with the XRD patterns due to the broadening and overlapping of the diffraction peaks. However, in the case of γ-Al_2O_3, the (4 0 0) reflection is the strongest and the relative intensity of the (4 0 0) and (3 1 1) peaks is 1.25, whereas for $Ni(Mg)Al_2O_4$, the (3 1 1) reflection is stronger and the relative peak intensity is 0.65. Besides, since Ni^{2+} (0.069 nm) and Mg^{2+} (0.072 nm) have ionic radii larger than Al^{3+} (0.057 nm), the diffraction peaks of $Ni(Mg)Al_2O_4$ spinel shift to smaller diffraction angles relative to those of γ-Al_2O_3.[53,54] Thus, the presence of $Ni(Mg)Al_2O_4$ can be identified by the variations in the relative intensity and the slight shift of the diffraction lines. Compared with 2θ = 45.6° and 66.4° for pure γ-MA,[45] the diffraction peaks of the (4 0 0) and (4 4 0) planes for γ-Al_2O_3 in the MgO/γ-MA sample in Fig. 1 shifted to smaller values at 2θ = 45.0 ° and 65.7°, respectively, and meanwhile, the relative intensity of the (4 0 0) and (3 1 1) peaks was ca. 0.99. This result demonstrated that parts of Mg^{2+} ions could diffuse into the lattices of γ-Al_2O_3 to form $MgAl_2O_4$. The addition of Ni^{2+} ions resulted in the further shifts to smaller 2θ values of the diffraction peaks, and concomitantly, the relative intensity of the (4 0 0) and (3 1 1) peaks showed an observable decline. This result implied that Ni^{2+} ions might react with alumina to produce $NiAl_2O_4$ spinel to a certain extent at 400 °C, likely due to homogeneous mixing and strong interaction between alumina and Ni^{2+} ions. The interaction of NiO with Al_2O_3 to form $NiAl_2O_4$ spinel on the alumina surface at relatively low temperatures (400–500 °C) was also reported in the documents.[55,56] From the XRD patterns in Fig. 1, with raising the Ni content to 21 wt %, the diffraction peaks of the (4 0 0) and (4 4 0) planes for MgO/γ-MA gradually shifted to 2θ angles at 44.4° and 64.8°, and the relative intensities of the (4 0 0) and (3 1 1) peaks declined to 0.85. These results implied that more Ni and/or Mg ions reacted with alumina to form $Ni(Mg)Al_2O_4$ with the increased Ni content. However, the relative intensities of the (4 0 0) and (3 1 1) peaks for the *x*NiO–MgO/γ-MA materials were always much higher than that (0.65) of $Ni(Mg)Al_2O_4$ spinel, even when the (Ni + Mg)/Al molar ratio exceeded 0.50. For example, the relative intensity of the (4 0 0) and (3 1 1) peaks for the 21NiO–MgO/γ-MA sample with a (Mg + Ni)/Al ratio of 0.628 was ca. 0.85. This result showed that only relatively small amounts of Ni^{2+} and Mg^{2+} ions were reacted to form $Ni(Mg)Al_2O_4$.[53]

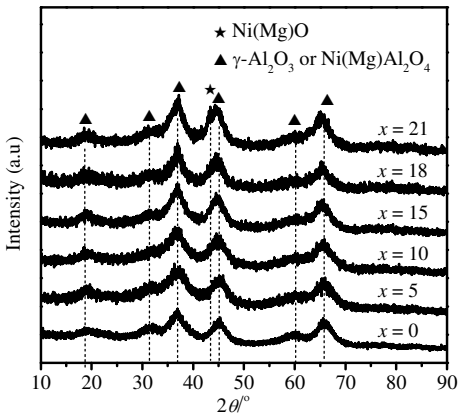

Fig. 1 XRD patterns of the xNiO–MgO/γ-MA materials.

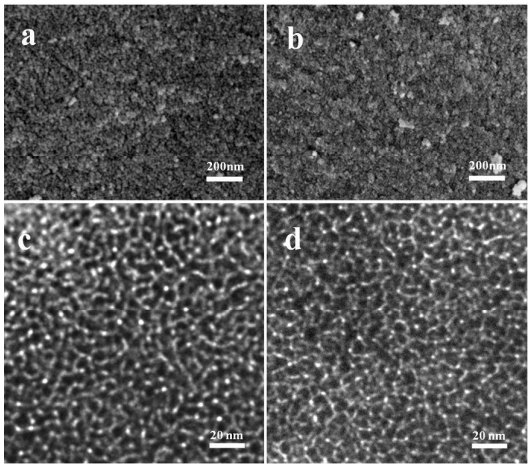

Fig. 2 SEM images of (a) 10NiO–MgO/γ-MA and (b) 21NiO–MgO/γ-MA, and TEM images of (c) 10NiO–MgO/γ-MA and (d) 21NiO–MgO/γ-MA.

Although the diffraction intensities for the *x*NiO–MgO/γ-MA materials in Fig. 1 increased with the increase in Ni content, the FWHMs of the diffraction lines showed little change. For example, FWHM for the (4 4 0) plane of MgO/γ-MA was 3.35°, while that of 21NiO–MgO/γ-MA only slightly decreased to 2.88°, correspondingly, the mean crystallite sizes from the Scherrer equation increased from 2.8 to 3.3 nm, which were only a bit larger than that (~2.5 nm) of pure γ-MA obtained at the same temperature of 400 °C.[44,45] These results suggested that the presence of Ni^{2+} ions along with Mg^{2+} ions had little influence on the crystalline structure and the crystallite sizes of γ-Al_2O_3, that is, the *x*NiO–MgO/γ-MA materials might still consist of small γ-Al_2O_3 and/or γ-Al_2O_3–$Ni(Mg)Al_2O_4$ nanoparticles, similar to pure γ-MA.[44]

3.1.2 SEM and TEM characterizations

The morphologies and mesoporous structures of the *x*NiO–MgO/γ-MA (*x* = 0, 5, 10, 15, 18, and 21) materials were characterized by SEM and TEM. Fig. 2(a) and (b) present the representative SEM images. The *x*NiO–MgO/γ-MA materials

were typically fabricated through the agglomeration of the cross-linking nanoparticles to form porous frameworks, similar to pure γ-MA.[44] This kind of inorganic porous materials with a cross-linking rigid skeleton via the non-surfactant sol-gel process was believed to have better heat and mass transfer properties than mesoporous materials of distinct particles obtained using surfactants.[57–59] The typical TEM images in Fig. 2(c) and (d) exhibited that the *x*NiO–MgO/γ-MA materials contained homogenous wormhole-like mesopores in the framework with the pore sizes of ca. 2.0–4.5 nm, close to that of pure γ-MA.[44] These results further confirmed that the presence of Ni^{2+} ions along with Mg^{2+} ions hardly affected both the crystalline γ-Al_2O_3 particle sizes and the mesoporous structure of γ-MA, in agreement with the XRD results in Fig. 1.

3.1.3 N_2 adsorption-desorption analysis

The physical properties of the *x*NiO–MgO/γ-MA materials (*x* = 0, 5, 10, 15, 18, and 21) were analyzed by N_2 adsorption-desorption measurements and the results are illustrated in Fig. 3. Similar to γ-MA,[44,45] all the *x*NiO–MgO/γ-MA materials exhibited characteristic type IV isotherms with apparent hysteresis loops, and contained mesopores of narrow pore size distributions in the range of 2.5–4.5 nm, as shown in the SEM and TEM images of Fig. 2. This result further supported that the gel precursors of the NH_4NO_3/Al species hybrids containing Ni^{2+} and Mg^{2+} ions could also be assembled into the mesoporous network structures during the thermal treatment process. However, the pore size distribution peaks were weakened due to the addition of Ni element.

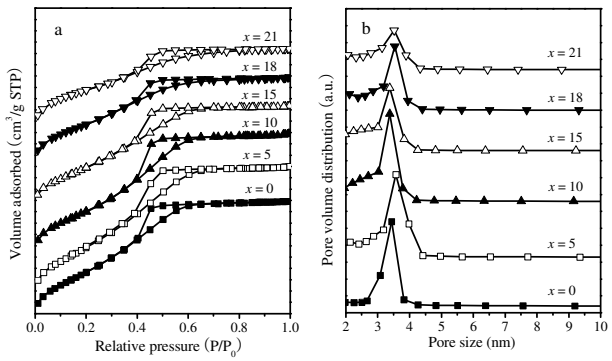

Fig. 3 (a) Nitrogen adsorption-desorption isotherms, and (b) BJH pore size distributions of the xNiO–MgO/γ-MA materials.

Table 1 Physical properties of the γ-MA and xNiO–MgO/γ-MA materials

Sample	S_{BET} ($m^2 g^{-1}$)	Vp ($cm^3 g^{-1}$)	Dp (nm)	Da (nm)
γ-MA	401	0.33	3.9	3.4
MgO/γ-MA	277	0.22	3.5	3.2
5NiO–MgO/γ-MA	249	0.21	3.6	3.2
10NiO–MgO/γ-MA	226	0.20	3.4	3.3
15NiO–MgO/γ-MA	213	0.18	3.5	3.3
18NiO–MgO/γ-MA	209	0.17	3.6	3.2
21NiO–MgO/γ-MA	200	0.15	3.5	3.2

The basic physical properties of the *x*NiO–MgO/γ-MA materials are listed in Table 1. Compared with pure γ-MA, the MgO/γ-MA material exhibited a clear decrease in specific surface area, pore volume and pore size. The addition of Ni resulted in the further decrease in specific surface area and pore volume, but pore sizes had little change. This could be mainly attributed to the reduction in the weight percentage of γ-MA with raising the Ni content. For instance, when the Ni content increased from 0 to 21 wt %, the S_{BET} and Vp for the MgO/γ-MA sample declined from 277 $m^2 g^{-1}$ and 0.22 $cm^3 g^{-1}$ to 200 $m^2 g^{-1}$ and 0.15 $cm^3 g^{-1}$ for the 21NiO–MgO/γ-MA sample by ca. 27% and 31%, respectively. On the other hand, the incorporation of NiO species into the pores of MgO/γ-MA and the interaction between MgO/γ-MA and NiO species could also have a certain effect on the specific surface areas, pore volumes and pore sizes.[14] The BJH peak pore sizes were all a bit larger than the average pore sizes (Da), implying that these materials contained small amounts of micropores.

3.1.4 XPS analysis

Fig. 4 and Table 2 present the XPS spectra of the Ni 2p regions and the corresponding BEs of the Ni $2p_{3/2}$ levels of the *x*NiO–MgO/γ-MA (*x* = 5, 10, 15, 18, and 21) materials, respectively. All the *x*NiO–MgO/γ-MA samples exhibited a Ni $2p_{3/2}$ primary peak positioned within a BE range of 855.5–855.1 eV, accompanied by a satellite peak at 861.4–861.0 eV. It was reported that the Ni $2p_{3/2}$ BEs were ~854.4 eV for pure NiO and ~857.3 eV for pure $NiAl_2O_4$, respectively.[60,61] This implicated that there existed the dispersed NiO species with an interaction with the support or a small amount of $NiAl_2O_4$ in the *x*NiO–MgO/γ-MA materials,[45] as exhibited in the XRD patterns of Fig. 1. With the increase in the Ni content from 5 to 18 wt %, the Ni $2p_{3/2}$ BEs gradually shifted from 855.5 eV to a smaller value of 855.1 eV. This result indicated that the interaction between NiO species and the support diminished, or the relative amount of NiO species to $NiAl_2O_4$ spinel increased with the Ni content. When the Ni content further increased, the BE value of the Ni $2p_{3/2}$ started to increase and showed a Ni $2p_{3/2}$ BE value at 855.3 eV for 21NiO–MgO/γ-MA.

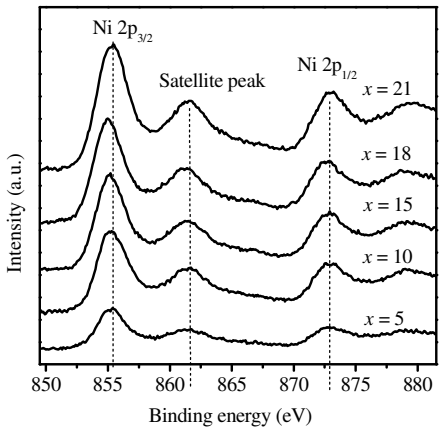

Fig. 4 Ni 2p XPS spectra of the *x*NiO–MgO/γ-MA materials.

Table 2 Ni $2p_{3/2}$ binding energies, surface compositions of Ni, Mg and Al elements of the xNiO–MgO/γ-MA samples

Sample	BE of Ni $2p_{3/2}$ (eV)	Composition by XPS (atomic ratio)		
		Ni/Al[a]	Mg/Al	(Ni+M)/Al
5NiO–MgO/γ-MA	855.5	0.043 (0.055)	0.362	0.405
10NiO–MgO/γ-MA	855.3	0.081 (0.117)	0.531	0.612
15NiO–MgO/γ-MA	855.2	0.099 (0.191)	0.814	0.913
18NiO–MgO/γ-MA	855.1	0.107 (0.242)	0.982	1.089
21NiO–MgO/γ-MA	855.4	0.120 (0.278)	0.751	0.871

[a] The values in parentheses are the nominal surface Ni/Al molar ratios.

Since the *x*NiO–MgO/γ-MA materials have very similar porous structures and pore size distributions, the elemental compositions estimated from the XPS spectra could basically reflect the variations in the element concentrations on the support surfaces.[38] Table 2 listed the surface atomic compositions of Ni and Mg relative to Al in the *x*NiO–MgO/γ-MA materials. Each sample showed much higher surface (Mg + Ni)/Al ratio than the corresponding nominal one for the *x*NiO–MgO/γ-MA. Generally, the (Mg + Ni)/Al ratio increased with raising Ni content, for example, 0.405 for 5NiO–MgO/γ-MA with the nominal (Mg + Ni)/Al ratio of 0.305, whereas 0.871 for 21NiO–MgO/γ-MA with the nominal (Mg + Ni)/Al ratio of 0.528. In combination with XRD patterns in Fig. 1, it could be inferred that Ni and Mg species were enriched on the surface of γ-MA support mainly in the form of highly dispersed NiO and MgO rather than incorporation into the lattices of γ-Al_2O_3 to form Ni(Mg)Al_2O_4; and only parts of the surface of γ-MA could be occupied by MgO and NiO species. The surface Ni/Al ratios increased with the Ni content, but were always much smaller the nominal values listed in parentheses. This result implied that NiO species might prefer to be anchored on the surface sites of γ-MA support; and MgO species were covered on the NiO species in the preparation procedure.[45] It is worth noting that the Mg/Al ratios also increased from 0.362 to 0.982 with the increase in the Ni content in the range of 5–18 wt %. However, when the Ni content was further increased, the Mg/Al ratio started to decline and presented a Mg/Al ratio of 0.751 for 21NiO–MgO/γ-MA. This result implicated that the presence of Ni resulted in larger surface of alumina to be occupied by MgO species with the Ni content to a certain extent. It seemed plausible to explain by the following aspects: due to the lower **s**olubility and solubility product constant (Ksp) of nickel hydroxide in aqueous solution, the increase in the Ni content generated more Ni hydroxide centres preferentially-deposited on the surface of the γ-MA support, where were more easily attached by Mg hydroxide species. As a result, the surface coverage of MgO species increased with the Ni content; on the other hand, with the increase in the MgO density on the surface of γ-MA, MgO species aggregated into larger MgO crystalline particles during the thermal treatment as displayed in Fig. 1, causing a decline in surface Mg/Al ratio.

3.1.5 CO_2-TPD measurement

The CO_2-TPD technique was used to analyze the influence of the Ni content on the strength and number of basic sites on the surfaces of the *x*NiO–MgO/γ-MA (*x* = 0, 5, 10, 15, 18, and 21) materials, and the CO_2-TPD profiles are displayed in Fig. 5. All the *x*NiO–MgO/γ-MA samples showed two distinct CO_2 desorption regions in the range of ca. 50–150 °C and 150–500 °C, respectively. This result was indicative of a heterogeneous distribution of basic site strength and the existence of different types of basic sites on the surfaces. The low-temperature CO_2 desorption centred at ca. 99 °C could be attributed to either the weakly chemisorbed CO_2 of the framework or the physically adsorbed CO_2.[34,45] The peak intensity gradually diminished with the increase in Ni content, showing a similar trend of the variations of the pore volumes and specific surface areas in Table 1. Regardless of Ni content, the CO_2 desorption for the strong basic sites in the range of 150–500 °C was always predominant for each sample, which could obviously be deconvoluted into two CO_2 desorptions peaked at ca. 274 °C and at 318–376 °C, respectively. In comparison with the CO_2-TPD profiles for MgO/γ-MA, the former was assigned to the MgO/γ-MA support, and the latter was associated with Ni oxide species. The medium-temperature CO_2 desorptions at ca. 274 °C for MgO/γ-MA had no discernible shift, but those associated with Ni oxide species gradually moved toward lower temperatures with increasing the Ni content to 18 wt%. In other words, the basic site strength of the Ni oxide species on the surfaces weakened with the increase in the Ni content. The XPS results in Table 2 indicated that the Ni contents on the surfaces increased, and the Ni $2p_{3/2}$ BEs gradually shifted to smaller values with the increase in the Ni content in the range of 0–18 wt%. Thus, it could be concluded that the combination and interaction between Ni oxide species and MgO/γ-MA support determined the higher basic site strength on the surface. When the Ni content further increased, the basic site strength of the Ni oxide species started to abate, and the CO_2 desorption peak became at 331 °C for 21NiO–MgO/γ-MA. This was likely due to the formation of MgO crystallites, weakening the interaction between the Ni oxide and Mg oxide species.

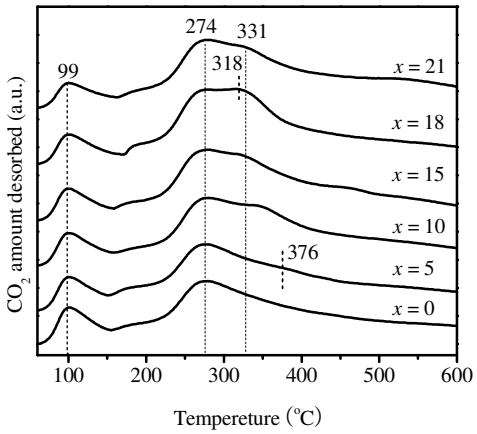

Fig.5 CO_2-TPD profiles for the *x*NiO–MgO/γ-MA materials.

Table 3 Relative amounts of CO_2 desorbed on the surfaces of *x*NiO–MgO/γ-MA samples in the range of 150−500 °C before and after the H_2 reduction

Sample	Amount of CO_2 desorbed relative to MgO/γ-MA[a]		Relative density of base sites (m^{-2})	
	Before reduction	After reduction	Before reduction [b]	After reduction [c]
MgO/γ-MA	100	65.5	0.36	0.29
5NiO–MgO/γ-MA	105.1	71.7	0.43	0.33
10NiO–MgO/γ-MA	111.9	83.4	0.49	0.45
15NiO–MgO/γ-MA	115.9	87.5	0.55	0.49
18NiO–MgO/γ-MA	125.5	92.0	0.61	0.56
21NiO–MgO/γ-MA	117.0	83.4	0.58	0.53

[a] Defined as the amount of CO_2 desorbed per gram of each catalyst divided by the amount of CO_2 desorbed (100 as the reference) per gram of MgO/γ-MA calcined at 400 °C in the range 150–500 °C. [b] The relative amount of CO_2 divided by the specific surface area of each catalyst before reduction. [c] The relative amount of CO_2 divided by the specific surface area of each catalyst after reduction at 600 °C.

Table 3 lists the total amounts of CO_2 desorbed for the strong basic sites relative to that (100 as the reference) of the MgO/γ-MA sample in the range of 150−500 °C and the corresponding amounts of CO_2 desorbed per unit surface area of the *x*NiO–MgO/γ-MA (*x* = 0, 5, 10, 15, 18, and 21) materials. It could be seen that both the total amount of CO_2 desorbed and the amount of CO_2 per unit surface area increased with raising Ni content and reached the maximum values at 18 wt % Ni content. These results demonstrated that the total number and the density of the basic sites augmented with the Ni content to a certain extent, in agreement with the change in the (Mg + Ni)/Al ratio on the surface with the Ni content in Table 2. With the further rise in Ni content, both the total number and the relative density of basic sites started to decline. This result could be mainly attributed to the decrease in the (Mg + Ni) composition on the surface due to the formation of larger MgO particles (Table 2).

3.2 Physicochemical properties of *x*Ni–MgO/γ-MA catalysts

3.2.1 H_2-TPR analysis of *x*NiO–MgO/γ-MA materials

H_2-TPR measurements were used to study the reducibility and the distribution of Ni species over the *x*NiO–MgO/γ-MA (*x* = 5, 10, 15, 18, and 21) materials. The H_2-TPR profiles are illustrated in Fig. 6. All the *x*NiO–MgO/γ-MA samples showed a predominating H_2 consumption and a weak H_2 consumption, the maximum values of which were positioned in the temperature ranges of 640–674 °C and 840–898 °C, respectively. The former was ascribed to the reduction of highly dispersed NiO species with an interaction with the support; and the latter was related to the reduction of bulk nickel aluminate-like species.[28,45] Both of the peak intensities increased with raising the Ni content, implicating that the increase in the Ni content augmented the amounts of not only dispersed NiO species but also nickel aluminate species, in line with the XRD patterns in Fig. 1. Generally, the H_2 consumption peaks for NiO shifted to lower reduction temperatures, whereas those for nickel aluminate moved toward higher temperatures with the increase in Ni content. This result implied that the interaction between NiO species and support abated with the increase in the Ni content. On the other hand, the incorporation of more divalent Ni^{2+} ions in the tetrahedral or octahedral sites in γ-Al_2O_3 resulted in a further decrease in the cationic deficiency of γ-Al_2O_3, rendering γ-Al_2O_3–Ni(Mg)Al_2O_4 more stable and elevating the reduction temperature of Ni^{2+} ions in spinel phase with raising Ni content.[62] For all the *x*NiO–MgO/γ-MA, no reduction peaks in the lower temperature region less than 500 °C were observed due to free and bulk-like NiO. This result further demonstrated that the Ni(Mg)O diffraction peaks for 21NiO–MgO/γ-MA in Fig. 1 were mainly due to crystalline MgO or Ni–Mg–O solid solution instead of bulk-like NiO.

It has been reported that not all Ni^{2+} ions were reducible in alumina-supported Ni catalysts.[38,45] The Ni content and the interaction of Ni^{2+} ions with the support might affect the coordination environments of Ni^{2+} ions, resulting in the variation in the reducibility of Ni^{2+} ions.[38] The reduction degree of Ni^{2+} ions was used to indicate the reducibility of Ni^{2+} ions in the *x*NiO–MgO/γ-MA (*x* = 5, 10, 15, 18, and 21) materials, and the results are summarized in Table 4. The reduction degrees of Ni^{2+} ions increased with raising Ni content and had a maximum value of 93.6% at 18 wt% Ni content. This result could match up with the XPS results in Fig. 4 and Table 2, which were determined by the combination of all the Ni^{2+} ions in NiO species and $NiAl_2O_4$ spinel. Therefore, the relative amounts of NiO to $NiAl_2O_4$, labeled as I(NiO)/I($NiAl_2O_4$), were also analyzed by deconvoluting the H_2 consumption curves for NiO and $NiAl_2O_4$, followed by the regional integration as shown for 5NiO–MgO/γ-MA in Fig. 6 as an example. As presented in Table 4, the relative amounts of NiO to $NiAl_2O_4$ increased with the increase in the Ni content in the range of 5−18 wt% due to the weakened interaction between Ni oxide species and alumina, causing the gradual decline in the Ni 2 $p_{3/2}$ BEs (Table 2). With further raising the Ni content to 21 wt%, the formation of larger MgO crystallite attenuated the interaction between NiO and MgO species, but improved the interaction between NiO and alumina. As a result, a larger relative amount of Ni^{2+} ions diffused into the γ-Al_2O_3 lattices to form $NiAl_2O_4$, resulting in an increase in the Ni $2p_{3/2}$ BE. It has been proven

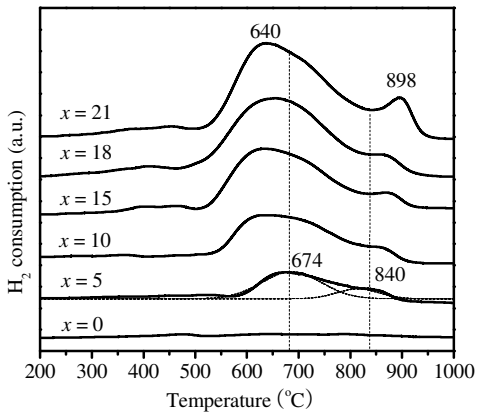

Fig. 6 H_2-TPR profiles for the *x*NiO–MgO/γ-MA materials.

Table 4 Degree of reduction of Ni^{2+}, relative amount of NiO species to $NiAl_2O_4$ spinel, and Ni crystallite sizes of the *x*Ni–MgO/γ-MA catalysts after H_2 reduction at 600 °C

Sample	Degree of reduction [a] (%)	I(NiO)/ I($NiAl_2O_4$)	Ni particle size (nm) by	
			XRD	TEM
5Ni–MgO/γ-MA	85.5	5.56	8.6	8.1 ± 0.9
10Ni–MgO/γ-MA	87.6	6.67	7.3	7.4 ± 0.8
15Ni–MgO/γ-MA	88.9	7.69	6.4	6.5 ± 0.8
18Ni–MgO/γ-MA	93.6	9.09	5.6	5.8 ± 0.8
21Ni–MgO/γ-MA	93.2	6.69	7.1	6.9 ± 0.9

[a] Defined as the percentage of the total molar amount of H_2 consumed for a sample to the molar amount of H_2 calibrated by CuO having the same molar amount of NiO in the sample between 200 and 1000 °C

that there were two forms of Ni^{2+} ions in the lattices of γ-alumina, i.e., the Ni^{2+} ions in the tetrahedral sites and the Ni^{2+} ions in the octahedral sites of γ-alumina. The former in the tetrahedral sites corresponds to "hard to reduce" nickel and the latter in the octahedral sites corresponds to "readily reduced" nickel.[38,63,64] Thus, it was proposed that the variation in the reduction degree might mainly due to the formation of $NiAl_2O_4$ spinel, in which some of the Ni^{2+} ions could react with the tetrahedral Al^{3+} sites or diffuse from the octahedral sites to tetrahedral sites of γ-alumina to form the inverse spinel structure at the moment when nickel ions interacted with the octahedral Al^{3+} sites to produce the normal spinel structure.[38,65] In addition, the dissolution of a tiny fraction of NiO into MgO to form Ni–Mg–O solid solution due to the strong interaction, which is more difficult to be reduced than $NiAl_2O_4$ spinel,[7,10] might also be responsible for the decrease in the reduction degree of Ni^{2+} ions.

3.2.2 XRD characterization of xNi–MgO/γ-MA catalysts

XRD measurements were applied to characterize the structure changes and metallic Ni crystallites formed in the NiO–MgO/γ-MA materials after the reduction with 20 vol % H_2/N_2 at 600 °C for 2 h, under which the obtained Ni–MgO/γ-MA catalysts were proved to be optimal for the steam reforming of LPG.[45,46] Fig. 7 illustrates the XRD patterns of *x*Ni–MgO/γ-MA (x = 5, 10, 15, 18, and 21) catalysts. For all the reduced catalysts, there appeared two new diffraction peaks at 51.9° and 76.4° corresponding to Ni (2 0 0) and (2 2 0) reflections, respectively, and a diffraction peak at ca. 44.5° associated with the Ni (1 1 1) plane, which was overlapped with the diffraction peak at ca. 45° corresponding to the (4 0 0) plane for γ-Al_2O_3. This result indicated that metallic Ni crystallites were formed in the *x*Ni–MgO/γ-MA samples. By carefully comparing the XRD patterns of the NiO–MgO/γ-MA materials before and after the reduction in Fig. 1 and Fig. 7, respectively, it could be found that the 2θ values, the relative intensities, and the shapes or the FWHMs of the diffraction peaks corresponding to γ-Al_2O_3 and/or Ni(Mg)Al_2O_4 had no observable changes except the (4 0 0) diffraction peaks overlapped with the Ni (1 1 1) reflection. This result implicated that $NiAl_2O_4$ could not be reduced at 600 °C, as exhibited in the TPR profiles of Fig. 6. The relative intensities of the Ni diffraction peaks gradually increased, but the peak widths were found to broaden with the Ni content in the range of 5–18 wt %. This result suggested that the Ni crystallite sizes decreased with the Ni content and had a minimum value at 18 wt % Ni content. In terms of 21Ni–MgO/γ-MA, the diffraction peak at 2θ = 43.3° corresponding to MgO disappeared, implying that the larger MgO crystallites on the surface were re-constructed into highly dispersed Mg species in the reduction processes. Table 4 summarizes the apparent Ni crystallite sizes estimated from the broadening of the Ni (2 0 0) reflection. When the Ni content increased from 5 to 18 wt %, the Ni crystallite sizes reduced from 8.6 to 5.6 nm. With the further increase in the Ni content, the Ni crystallite size started to increase, and showed an apparent Ni crystallite size of 7.1 nm for the 21Ni–MgO/γ-MA catalyst. Generally speaking, the strong interaction between metal oxide species and support improves the attachment of the reduced metal to form stable metal nanoparticles with relatively high dispersion in the reduction process. However, the H_2-TPR profiles in Fig. 6 showed that the interaction between NiO species and support weakened with the Ni content. Although such an abnormal phenomenon was also observed in the other study,[29] there has not been a reasonable and widely-accepted explanation on it up to now. It was proposed here that the variations in Ni crystallite sizes with the Ni content for the *x*Ni–MgO/γ-MA catalysts should be attributed to a combination of several factors, including the physical properties, the reduction rate of NiO species, the interaction between Ni crystallites and support, the metallic Ni content, and the reduction temperature. In the case of the *x*NiO–MgO/γ-MA samples with low Ni contents, the NiO species had the higher reduction temperatures due to the stronger interaction with the support, the reduction rate of the NiO species was lower and became the rate-determining step, in which Ni atoms or small Ni clusters were released very slowly for the growth of metallic Ni crystallites. The Ni atoms and/or Ni clusters with high surface energies could overcome the pore confinement and attachment effects of the support to move toward the small Ni crystallites initially formed in the framework and produce larger Ni crystallites. In this case, Ostwald ripening, namely monoatomic species or small clusters diffuse from small to larger particles,[39] might be the dominant mechanism for Ni crystallite growth rather than migration and coalescence of Ni

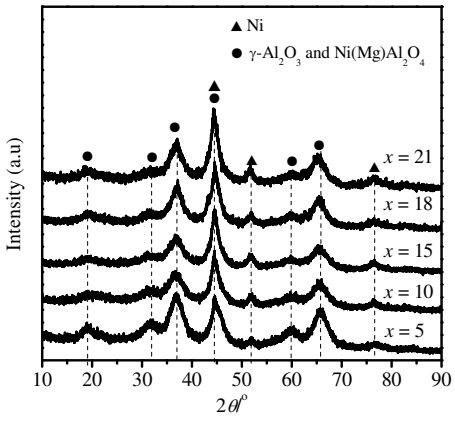

Fig. 7 XRD patterns of the *x*Ni–MgO/γ-MA samples.

nanoparticles. With the further increase in the Ni content, the reduction rate of the NiO species became so speedy that they could be rapidly reduced into metallic Ni atoms or small Ni clusters supersaturated on the support surface due to the higher surface density of NiO species, coalescing to form uniformly metallic Ni crystallites with medium sizes confined by pore structures during a short time. At the appropriate reduction temperature, the free energy released by the growth was insufficient for driving the medium-size Ni crystallites to migrate on the surface and to form larger particles in the cross-linking framework. In terms of the 21Ni–MgO/γ-MA, the density of Ni nanocrystallites on the surface was so high that they could grow up to become larger Ni crystallites by migration and coalescence of Ni nanoparticles.

3.2.3 TEM analysis of xNi–MgO/γ-MA catalysts

Fig. 8 displays the TEM images and the corresponding Ni particle size distributions of the *x*Ni–MgO/γ-MA (*x* = 5, 10, 15, 18 and 21) catalysts after the H_2 reduction at 600 °C. All the *x*Ni–MgO/γ-MA catalysts showed homogeneous wormhole-like mesoporous structures with pore sizes of ca. 2.0–5.0 nm, which were very similar to those before the reduction. The Ni nanoparticles were homogeneously dispersed with relatively narrow particle size distributions in the mesoporous frameworks. The dispersion densities of the Ni particles in the support frameworks increased clearly with increasing the Ni content from 5 to 18 wt %, then showed a decrease for the 21Ni–MgO/γ-MA sample due to the growth of Ni particles. Table 4 lists the mean sizes and standard deviations of the Ni particles in the TEM images. The Ni particle sizes gradually decreased from 8.1 to 5.8 nm with increasing the nickel content from 5 to 18 wt %, but became 6.9 nm at 21 wt % Ni content, in good agreement with the XRD results in Table 4.

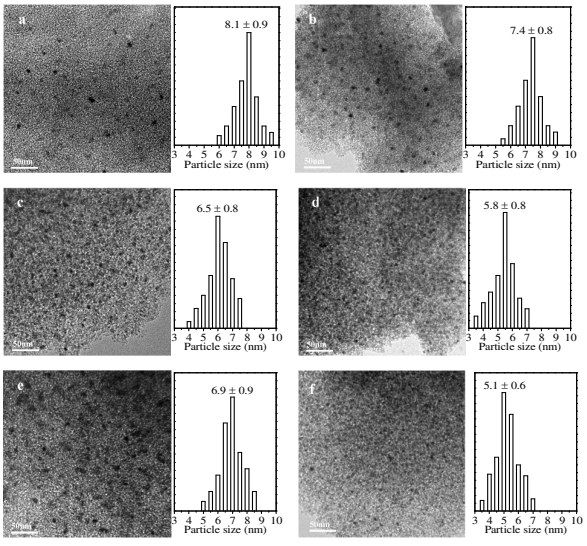

Fig. 8 TEM images and corresponding Ni particle size distributions of the *x*Ni–MgO/γ-MA catalysts. (a) *x* = 5%, (b) *x* = 10%, (c) *x* = 15%, (d) *x* = 18%, (e) *x* = 21%, and (f) spent 18Ni–MgO/γ-MA–*S* after steam reforming of LPG at 450 °C for 40 h.

Table 5 Physical properties of the *x*Ni–MgO/γ-MA catalysts after H_2 reduction at 600 °C

Sample	S_{BET} ($m^2\ g^{-1}$)	Vp ($cm^3\ g^{-1}$)	Dp (nm)	Da (nm)
MgO/γ-MA	229	0.19	3.4	3.4
5Ni–MgO/γ-MA	221	0.18	3.5	3.9
10Ni–MgO/γ-MA	183	0.17	3.4	3.8
15Ni–MgO/γ-MA	180	0.16	3. 4	3.7
18Ni–MgO/γ-MA	167	0.16	3.6	3.7
21Ni–MgO/γ-MA	159	0.16	3.6	3.7

3.2.4 N_2 adsorption-desorption of *x*Ni–MgO/γ-MA catalysts

All the *x*Ni–MgO/γ-MA (*x* = 5, 10, 15, 18, and 21) catalysts after the H_2 reduction at 600 °C exhibited the similar shape N_2 sorption isotherms and pore size distributions (not shown) to the counterparts before the reduction in Fig. 3. This was an indication that the mesoporous frameworks of *x*NiO–MgO/γ-MA were still maintained after the reduction, as exhibited in the TEM images of Fig. 8. However, the *x*Ni–MgO/γ-MA catalysts in Table 5 generally presented smaller specific surface areas and pore volumes than the corresponding *x*NiO–MgO/γ-MA precursors in Table 1. This result could be attributed to the variations in the physical properties caused by the higher reduction temperature.[45] The N_2 sorption measurements of the *x*NiO–MgO/γ-MA samples calcined at 600 °C could confirm this point, as an example, the S_{BET} and Vp of the 18NiO–MgO/γ-MA sample calcined at 600 °C reduced to 165 $m^2\ g^{-1}$ and 0.14 $cm^3\ g^{-1}$, respectively.[46] In contrast to those before the reduction, the *x*Ni–MgO/γ-MA catalysts showed a bit smaller BJH pore size than the average pore size. This indicated that the micropores in the *x*Ni–MgO/γ-MA decreased, likely due to a combination of the reduction of NiO species, structural shrinkage as well as blockage of micropores in the reduction process.

3.2.5 CO_2-TPD analysis of *x*Ni–MgO/γ-MA catalysts

Fig. 9 illustrates the CO_2-TPD profiles of the *x*Ni–MgO/γ-MA (*x* = 0, 5, 10, 15, 18, and 21) catalysts after the reduction at 600 °C. Similar to the *x*NiO–MgO/γ-MA in Fig. 5, the *x*Ni–MgO/γ-MA also exhibited two distinct CO_2 desorption regions. However, the former for the weak basic sites was still peaked at 99 °C, whereas the latter associated with the strong basic sites in the range of 150–500 °C involved only one CO_2 desorption peaked at ca. 274 °C, although it was still predominant. These results indicated that the Ni oxide species were reduced into metallic Ni, and the *x*Ni–MgO/γ-MA had the same strength of basic sites. Compared with before the reduction, the *x*Ni–MgO/γ-MA exhibited smaller peak intensity and narrower peak width of the low-temperature CO_2 desorption due to the decrease in pore volume, specific surface area, and micropores (Table 5).

The amounts of CO_2 for the strong basic sites over the *x*Ni–MgO/γ-MA and the corresponding densities of basic sites on the surfaces are also given in Table 3 for comparison. In the case of the MgO/γ-MA, either the amount of CO_2 or the density of basic sites showed a discernible decrease. This result indicated that the reduction atmosphere and higher reduction temperature lowered not only the pore volume and

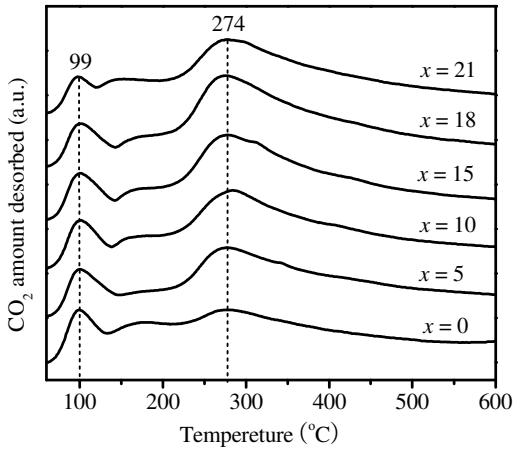

Fig. 9 CO_2-TPD profiles for the *x*Ni–MgO/γ-MA catalysts.

specific surface area but also the number of strong basic sites on the catalyst surface. For the *x*Ni–MgO/γ-MA (*x* = 5, 10, 15, 18, and 21), both the amounts of CO_2 and the corresponding densities of strong basic sites were smaller than those for the counterparts before the reduction mainly due to the reduction of NiO species to metallic Ni. In addition, the reduction atmosphere and temperature might also have a certain effect on the number and density of basic sites. It was noteworthy that the amounts of CO_2 for the *x*Ni–MgO/γ-MA presented a very similar trend to those before the reduction with the increase in Ni content. This result implied that the MgO surface concentrations on γ-MA support in the *x*Ni–MgO/γ-MA also increased with the Ni content and reached the maximum at 18 wt% Ni content; in other words, the distribution of MgO on the surface after the reduction had no significant change.

3.2.6 H_2 chemisorption analysis of *x*Ni–MgO/γ-MA catalysts

Hydrogen chemisorption was performed to analyze the surface areas of metallic Ni available in the *x*Ni–MgO/γ-MA (*x* = 5, 10, 15, 18, and 21), and the results are listed in Table 6. The amounts of hydrogen uptakes were augmented with increasing Ni content and showed a maximum value. As a result, the surface areas of metallic Ni increased from 3.97 to 21.45 $m^2\ g_{cat}^{-1}$ with the increase in the Ni content from 5 to 18 wt %, and then declined to 17.45 $m^2\ g_{cat}^{-1}$ at 21 wt % Ni content. These results were consistent with the variations in the Ni crystallite size with the Ni content shown in the XRD and TEM results in Table 4.

3.3 Pre-reforming of LPG over *x*Ni–MgO/γ-MA catalysts

The influence of the Ni content on the catalytic properties of the *x*Ni–MgO/γ-MA (*x* = 5, 10, 15, 18, and 21) catalysts was investigated for the pre-reforming of LPG at 450 °C and GHSV of 3.5×10^4 mL $g_{cat}^{-1}\ h^{-1}$ (STP) with a steam to carbon molar ratio (S/C) of 2.0. The activities as a function of reaction time are presented in Fig. 10. It could be seen that the Ni content significantly affected the activity and stability of the *x*Ni–MgO/γ-MA catalysts. The 5Ni–MgO/γ-MA catalyst showed the

Table 6 Hydrogen chemisorption results, initial LPG conversions, and corresponding TOFs over the *x*Ni–MgO/γ-MA catalysts for the steam reforming of LPG

Sample	H_2 uptake (μmol g_{cat}^{-1})	Ni surface area ($m^2\ g_{cat}^{-1}$)	X_{LPG} (%)	TOF (h^{-1})
5Ni–MgO/γ-MA	50	3.97	8.3[a]	262
10Ni–MgO/γ-MA	111	8.61	8.9	269
15Ni–MgO/γ-MA	216	16.79	16.6	261
18Ni–MgO/γ-MA	250	21.45	20.3	272
21Ni–MgO/γ-MA	223	17.45	17.4	264

[a] Reaction conditions: S/C, 2; SV, 1.5×10^5 mL $g_{cat}^{-1}\ h^{-1}$; reaction temperature, 450 °C, reaction time, 1 h

poorest initial LPG conversion of 31.3%. With raising the nickel content, the initial conversions of LPG increased and exhibited a maximum value of 97.8% at 18 wt % Ni content. When the nickel content further increased to 21 wt %, the initial conversion of LPG declined to 95.6%. These results were consistent well with the changes in the metal Ni surface area in Table 6, namely, the *x*Ni–MgO/γ-MA catalyst with a higher Ni surface area also possessed a higher initial conversion of LPG. It was demonstrated that the *x*Ni–MgO/γ-MA catalysts had similar porous frameworks with almost the same pore sizes and pore size distributions, which could be presumed to have approximate kinetics of heat transfer and mass transport in the reaction process; while the number and density of strong basic sites generally increased with the Ni content, which were considered to inhibit the steam reforming of hydrocarbons. Thus, it could be concluded that there was a close relationship between the catalytic activities and Ni surface areas available; and the improved activities with the Ni contents were mainly attributed to the increases in Ni surface areas.

The previous investigations indicated that the addition of MgO and the appropriate calcination temperature could improve the activities of the Ni–MgO/γ-MA catalysts for the pre-reforming of LPG mainly by affecting the crystallite sizes of metallic Ni formed.[45,46] In order to gain a deep insight into the interrelations among the Ni active sites, the catalytic activities, and the surface properties of the *x*Ni–MgO/γ-MA (*x* = 5, 10, 15, 18, and 21) catalysts, we further discussed the TOFs for the pre-reforming of LPG. Taking into account the catalyst stability, the TOFs were estimated by the initial LPG conversions at 1 h. Table 6 summarizes the initial conversions of LPG and the corresponding TOFs over the *x*Ni–MgO/γ-MA for the pre-reforming of LPG at 450 °C and SV of 3.3×10^5 mL $g_{cat}^{-1}\ h^{-1}$ with the S/C of 2.0, unless specified otherwise. The initial conversions of LPG were found to present the same trend as the Ni surface areas, that is, the initial LPG conversions were in proportion to the number of Ni active sites available. As a consequence, the TOFs of Ni active sites were almost the same at ca. 261–272 h^{-1} for all the *x*Ni–MgO/γ-MA catalysts. It has been known that the *x*Ni–MgO/γ-MA catalysts had almost the same pore sizes and pore size distributions, but the specific surface areas and pore volumes decreased with raising the Ni content. Therefore, it could further be demonstrated that the number of Ni active sites available on the surface was mainly responsible for the activity of the Ni–MgO/γ-MA catalysts for the pre-reforming of LPG; and there was no significant

relationship among the catalytic activities, the specific surface areas, and pore volumes.

The stability of the *x*Ni–MgO/γ-MA was also significantly influenced by the Ni content for the pre-reforming of LPG as shown in Fig. 10. The 5Ni–MgO/γ-MA catalysts exhibited the poorest stability in the LPG reforming. The LPG conversion gradually declined from the initial 31.3% to 13.3% by a deactivation degree of 57.5% during the tested reaction time of 40 h (Deactivation degree = (Initial LPG conversion – Final LPG conversion)/Initial LPG conversion × 100%). With raising the Ni content, the stability of the *x*Ni–MgO/γ-MA rapidly increased, for example, during the 40-h reaction, the deactivation degrees of the 10Ni–MgO/γ-MA and 15Ni–MgO/γ-MA catalysts were 20.4% and 4.2%, respectively. When the Ni content increased to 18 wt %, the LPG conversion kept unchanged at ca. 97% in the entire 40-h reaction process. The further increase in the Ni content gave rise to a decrease in the catalyst stability once again, and at 21 wt% Ni content, the LPG conversion reduced from the initial 95.6% to 88.5 % with a deactivation degree of 7.5% at 40 h. These results were well consistent with the surface areas and the crystallite sizes of metallic Ni. It has been demonstrated in Table 6 that the TOFs of metallic Ni active sites were almost the same for the pre-reforming of LPG. Therefore, it was plausible that the Ni crystallite sizes should be mainly responsible for the catalytic stability; and smaller Ni particles could greatly improve the stability of the *x*Ni–MgO/γ-MA catalysts in addition to providing more Ni active sites. It was reported that the carbon formation was a structure-sensitive reaction and the rate of coke deposition strongly depended on the Ni crystallite sizes.[66,67] In the case of Ni-based catalysts, the surface carbons were generally accepted as the key reaction intermediates for the reforming of hydrocarbons.[25,65] The surface carbon atoms could not only react with surface oxygen atoms to form CO and/or CO_2 but also combine with other surface carbon atoms to generate coke deposition. However, the formation of the carbidic carbon (*C), a precursor of the inert carbon causing the deactivation of Ni-based catalysts, required an ensemble of higher synergetic Ni active sites than the gasification of CH_x ($1 \le x \le 3$) species.[67,68] Therefore, the larger Ni crystallites more benefited the coke deposition, whereas the smaller Ni particles prevented CH_x species from occupying the proper active sites to form *C, resulting in a decrease in the rate of carbon deposition.[24,45,66] On the other hand, the improved stability might be also related to the variation in the surface basicity with the Ni content, as summarized in Table 3.

Fig. 11 presents the selectivities of the products (CH_4, CO_2, CO, and H_2) along with the LPG conversions over the *x*Ni–MgO/γ-MA (*x* = 5, 10, 15, 18, and 21) catalysts for the pre-reforming of LPG after the 40-h reaction time. The CH_4 selectivities were observed to have a similar trend of variation to the LPG conversions, while the opposite was true for those of CO_2, CO and H_2. This result indicated that the *x*Ni–MgO/γ-MA with a high activity for the steam reforming of LPG should also be was highly active for the formation of methane.

$C_nH_m + H_2O \rightarrow CO_x + H_2 \quad \Delta H° > 0$ ($n \ge 2$ and $x = 1$ or 2) (1)

$CO + 3H_2 \leftrightarrow CH_4 + H_2O \quad \Delta H° = -205.9$ kJ/mol (2)

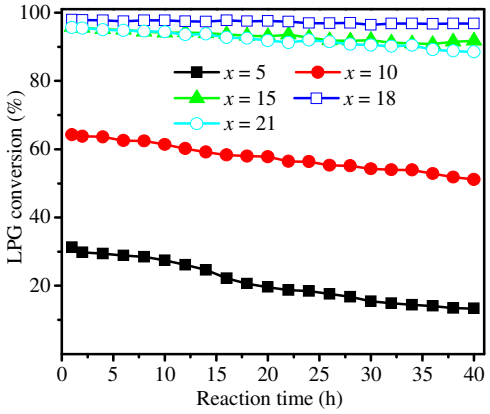

Fig. 10 Activities as a function of reaction time over the *x*Ni–MgO/γ-MA catalysts for the steam reforming of LPG.

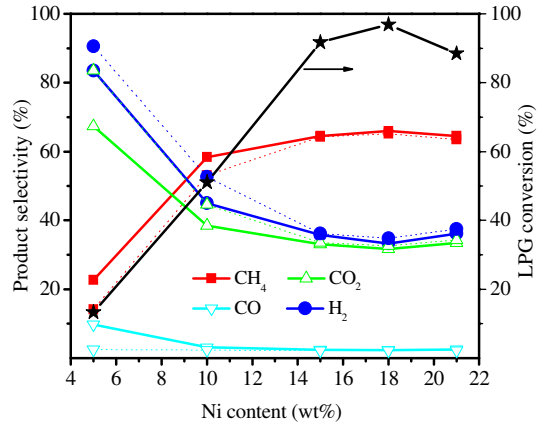

Fig. 11 LPG conversions and product selectivities (solid line) of the *x*Ni–MgO/γ-MA catalysts and the estimated equilibrium values of product selectivities (dot line) for the steam reforming of LPG.

$CO_2 + 4H_2 \leftrightarrow CH_4 + 2H_2O \quad \Delta H° = -164.7$ kJ/mol (3)

$CO + H_2O \leftrightarrow CO_2 + H_2 \quad \Delta H° = -41.2$ kJ/ (4)

$C_nH_m + (2n-m/2)H_2 \rightarrow nCH_4 \quad \Delta H° < 0$ (5)

The steam reforming of all higher hydrocarbons (n ≥ 2) (Eq. 1) could be considered as a thermodynamically irreversible process.[19] This meant that the pre-reforming of LPG over the *x*Ni–MgO/γ-MA catalysts was controlled by reaction kinetics under the present operating conditions. In order to analyze the effect of the Ni content on the product distribution, methanation of CO and CO_2 (Eqs. 2 and 3), and water gas shift (Eq. 4) over the *x*Ni–MgO/γ-MA catalysts in the pre-reforming of LPG, the theoretical values of the product selectivities (CH_4, CO_2, CO, and H_2) at the thermodynamic equilibrium, which were estimated on the basis of the total small gas molecules (CO, CH_4, H_2, CO_2, and H_2O) except LPG in the exit gas, are also presented in Fig. 11. It could be seen that the selectivities to CH_4 were more than the corresponding equilibrium values over the *x*Ni–MgO/γ-MA (*x* = 5 and 10). This result suggested that parts of methane was generated from the hydrocracking of LPG (Eq. 5), besides the methanation of CO and/or CO_2 with H_2. This phenomenon was also observed over hydrotalcite-

derived Mg–Al mixed oxide supported Ni catalysts,[10] and γ-MA-supported Ni–MgO catalysts with lower Mg contents and obtained at a higher calcination temperature of 700 °C for the steam reforming of LPG.[45,46] In Fig. 11, the CO selectivities were higher than the corresponding equilibrium values, and the CO_2 selectivities were lower than the equilibrium values, when the Ni content was less than 15%. This result indicated that the water gas shift was controlled by kinetics over the *x*Ni–MgO/γ-MA catalysts with lower Ni contents. When the Ni content was further increased, the selectivities of CO, CO_2 and CH_4 were very close to the equilibrium values, implying that both the methanation of CO and CO_2 and water gas shift reached the chemical equilibrium in the reaction system. This result meant that the increase in Ni content prevented the hydrocracking of LPG, but promoted the methanation of CO and/or CO_2 and water gas shift. The previous studies[45,46] demonstrated that the addition of Mg in the Ni–MgO/γ-MA catalysts improved the basic properties on the catalyst surface, inhibiting the hydrocracking of LPG, however, water gas shift and the methane of CO and CO_2 were related with not only surface basic properties but also the Ni particle sizes. Therefore, it could be proposed that in the *x*Ni–MgO/γ-MA catalysts with lower Ni contents, the low coverage of MgO or less number of basic sites on the support surface and the larger Ni crystallites more favored the hydrocracking of LPG to form CH_4 and further deep cracking of CH_x to produce coke deposition; on the other hand, more number of basic sites and smaller Ni crystallites on the surface might contribute to the methanation of CO and/or CO_2 with H_2 and water gas shift reaction.[24,45,66] These results also demonstrated that the pre-reforming of hydrocarbons over Ni-based catalysts was rather complicated, but the catalytic properties could be improved by modifying supports, selecting promoters, and improving preparation routes.

3.4 Characterization and discussion of spent *x*Ni–MgO/γ-MA catalysts

Fig. 12 illustrates the XRD profiles of the *x*Ni–MgO/γ-MA–*S* (*x* = 5, 10, 15, 18, and 21) catalysts for the pre-reforming of LPG at 450 °C after the 40-h reaction time. The *x*Ni–MgO/γ-MA–*S* catalysts showed almost the same XRD diffraction patterns corresponding to the γ-Al_2O_3 and/or γ-Al_2O_3–Ni(Mg)Al_2O_4 as the counterparts before the reaction, and no additional diffraction lines due to transition alumina and MgO and/or NiO phases were observed. These results indicated that no phase transformation took place, and the mesoporous γ-Al_2O_3 frameworks might still be maintained. However, the Ni peak intensities were weakened and more diffused, relative to those before the reaction. This result meant that the reaction atmosphere could influence the interaction between the Ni particles and the support, resulting in the re-construction of the Ni crystallites in the ptr-reforming of LPG.[7,14] Table 7 summarizes the apparent Ni crystallite sizes over the *x*Ni–MgO/γ-MA–*S* catalysts for the pre-reforming of LPG. The mean sizes of the Ni crystallites became a bit smaller compared with those before the reaction in Table 4. For example, the mean size of the Ni crystallites for 18Ni–MgO/γ-MA–*S* turned to 5.1 nm from 5.6 nm for 18Ni–MgO/γ-MA. It was proposed that the reversible reduction-oxidation between metallic Ni atoms and Ni^{2+} ions on the catalyst surface should have come about during the steam reforming of LPG. As a result, the Ni species were re-constructed or re-distributed, and even small parts of metallic Ni were re-oxidized to NiO species, producing metallic Ni particles dispersed more finely.[7,14,46] In Fig. 12, there was no clear diffraction peaks observed at 26.2°, corresponding to graphitic carbon (PDF 26–1080).

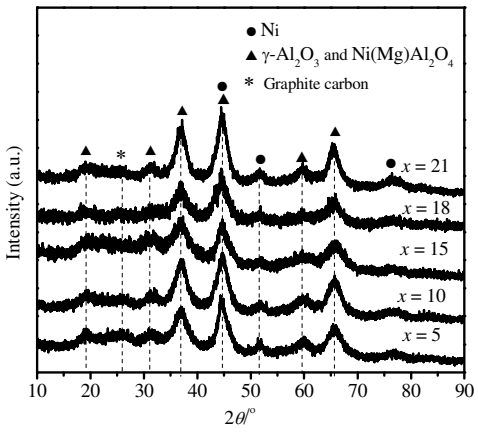

Fig. 12 XRD patterns of the spent xNi–MgO/γ-MA–S catalysts for the steam reforming of LPG.

The TEM images of the *x*Ni–MgO/γ-MA–*S* showed similar frameworks with a homogenous mesoporous structure to those before the reaction in Fig. 8(a)–(e). The representative TEM image of 18Ni–MgO/γ-MA–*S* is illustrated in Fig. 8(f). It could be seen that the Ni nanoparticles were uniformly distributed in the support frameworks, just as before the reaction. However, as summarized in Table 7, the sizes of the Ni nanoparticles after the reaction turned slightly smaller than those before the reaction, which were consistent with the XRD results also presented in Table 7.

Maintenance of the mesoporous structures in the spent *x*Ni–MgO/γ-MA–*S* catalysts was also evidenced by the N_2 sorption measurements (not shown). All the *x*Ni–MgO/γ-MA–*S* catalysts displayed the similar shape N_2 sorption isotherms and pore size distribution curves to the counterparts before the reaction. Table 7 gives the specific surface areas, pore volumes and pore sizes of the *x*Ni–MgO/γ-MA–*S* catalysts, which were observed to be close to those before the reaction in Table 5. These results further indicated that the *x*Ni–MgO/γ-MA catalysts had very high structure stability for the pre-reforming of hydrocarbons.

Table 7 summarizes the amount of deposited carbon on the *x*Ni–MgO/γ-MA–*S* (*x* = 5, 10, 15, 18, and 21) catalysts estimated from 500 to 800 °C in the TG profiles. Except that over the 5Ni–MgO/γ-MA–*S* with very low initial LPG conversion, the amounts of carbon deposited over other *x*Ni–MgO/γ-MA–*S* catalysts lowered with the increase in the Ni content and reached a minimum value of 55 mg g_{cat}^{-1} at 18 wt

% Ni content. However, regardless of the Ni content, the percentages of the deposited carbon to the converted carbon in LPG during the reaction period of 40 h (designated as P_{carbon}) seemed to fit in with the variations in the catalyst stabilities with the Ni content. The previous characterizations have confirmed that Ni particle sintering and phase transformation of alumina in the *x*Ni–MgO/γ-MA catalysts did not take place in the pre-reforming of LPG. Therefore, it could be concluded that the coke deposition on the surface was the most important factor for the catalyst deactivation; whereas the sizes of Ni particles played a decisive role for the rate of coke deposition, affecting the activity and stability of the Ni catalyst. It was noteworthy that the 15NiO–MgO/γ-MA catalyst with a smaller average Ni crystallite size of 6.5 nm showed larger amount of carbon than the 21NiO–MgO/γ-MA catalyst with a Ni crystallite size of 6.9 nm (Table 4) did. This result implied that the basicity on the surface of the *x*Ni–MgO/γ-MA catalysts might have a certain role in the coke deposition for the steam reforming of hydrocarbons.

Table 7 Ni particle sizes and deposited carbon, and physical properties over the spent *x*Ni–MgO/γ-MA catalysts for the pre-reforming of LPG[a]

Sample	Ni particle size (nm) by		S_{BET} ($m^2\ g^{-1}$)	Vp ($cm^3\ g^{-1}$)	Dp (nm)	Da (nm)	Carbon amount by TG (mg g_{cat}^{-1})	P_{carbon} (%)
	XRD	TEM						
5Ni–MgO/γ-MA–*S*	7.4	6.5 ± 0.7	220	0.16	3.4	3.5	86	0.252
10Ni–MgO/γ-MA–*S*	6.4	5.9 ± 0.6	206	0.16	3.5	3.6	105	0.126
15Ni–MgO/γ-MA–*S*	5.3	5.2 ± 0.5	183	0.15	3.5	3.7	81	0.055
18Ni–MgO/γ-MA–*S*	5.1	5.0 ± 0.5	163	0.15	3.5	3.6	55	0.035
21Ni–MgO/γ-MA–*S*	6.2	5.8 ± 0.6	153	0.16	3.4	3.4	71	0.050

[a] Reaction conditions: S/C, 2; SV, 3.5×10^4 mL $g_{cat}^{-1}\ h^{-1}$; reaction temperature, 450 °C, reaction time, 40 h.

4. Conclusions

Mesoporous γ-alumina-supported Ni–Mg oxides (*x*NiO–MgO/γ-MA) with various nickel contents (*x* = 0, 5, 10, 15, 18, and 21) were prepared through one-pot hydrolysis and co-condensation of inorganic salts. All the *x*NiO–MgO/γ-MA materials showed similar mesoporous frameworks through the cross-linking of small γ-Al_2O_3 and/or γ-Al_2O_3–Ni(Mg)Al_2O_4 nanoparticles with high specific surface areas and narrow pore size distributions. The specific surface areas and the pore volumes lowered with the nickel content. Ni species were homogeneously distributed in mesoporous γ-alumina frameworks mainly in the form of highly dispersed NiO. The interaction between Ni species and support attenuated with the increase in the Ni content in the range of 0–18 wt %, resulting in the gradual increases in the relative amount of NiO species to $NiAl_2O_4$ spinel and the reduction degree of Ni^{2+} ions. The surface Mg/Al ratios enhanced with the Ni content and showed a maximum value at 18 wt % Ni content, which were consistent with the numbers and surface densities of basic sites. After the H_2 reduction at 600 °C, the *x*Ni–MgO/γ-MA catalysts produced uniformly dispersed Ni nanoparticles with relatively narrow particle size distributions in the support frameworks. However, the Ni particle sizes decreased with the increase in the Ni content in the range of 5–18 wt %. This phenomenon could be explained by the dominant mechanism for the Ni crystallite growth by Ostwald ripening. The catalytic properties of the *x*Ni–MgO/γ-MA catalysts for the pre-reforming of LPG showed that the Ni contents strongly affected the catalytic activity and stability and resistance to coke deposition, mainly by the changes in the surface areas and the sizes of Ni crystallites. Smaller metallic Ni nanoparticles could facilitate the steam reforming of LPG and the subsequent methanation of CO and CO_2 with H_2 and water gas shift, but prevent the hydrocracking of LPG and lower the formation rate of coke deposition.

Acknowledgements

This research was supported by Innovation Program of Shanghai Municipal Education Commission, the Major State Basic Research Development Program of China (No. 2014CB643403), National Science Fund for Distinguished Young Scholars (No. 51225401) and Basic Major Research Program of Science and Technology Commission Foundation of Shanghai (No. 14JC1491400).

Notes and references

1 J. Tollefson, *Nature,* 2010, **464**, 1262–1264.
2 D.L. Trimm and Z.I. Onsan, Catal. *Rev. Sci. Eng.,* 2001, **43**, 31–84.
3 B. Valle, B. Aramburu, A. Remiro, J. Bilbao and A.G. Gayubo, *Appl. Catal., B* 2014, **147**, 402–410.
4 D. Baudouin, U. Rodemerck, F. Krumeich, A. de Mallmann, K.C. Szeto, H. Ménard, L. Veyre, J.P. Candy, P.B. Webbd, C. Thieuleux and C. Copéret, *J. Catal.,* 2013, **297**, 27–34.
5 C.B. Karin, J. Radnik and E.V. Kondratenko, *J. Catal.,* 2011, **280**, 116–124.
6 G.P. Szijjártó, Z. Pászti, I. Sajó, A. Erdohelyi, G. Radnóczi and A. Tompos, *J. Catal.,* 2013, **305**, 290–306.
7 K. Takehira, T. Shishido, P. Wang, T. Kosaka and K. Takaki, J. Catal., 2004, **221**, 43–54.
8 C.S. Song, *Catal. Today*, 2002, **77**, 17–49.
9 S. Park, D.R. Park, J.C. Jung, J.S. Chung and I.K. Song, *Catal. Today,* 2009, **146**, 44–49.
10 K. Shen, X.G. Wang, X.J. Zou, X.X. Wang, X.G. Lu and W.Z. Ding, *Int. J. Hydrogen Energy*, 2011, **36**, 4908–4916.
11 K. Nagaoka, K. Sato and Y. Takita, *J. Catal.*, 2012, **287**, 86–92.
12 H. Jeong and M. Kang, *Appl. Catal. B,* 2010, **95**, 446–455.
13 Y. Lu, J.C. Chen, Y. Liu, Q.S. Xue and M.Y. He, *J. Catal.,* 2008, **254**, 39–48.
14 X.J. Zou, X.G. Wang, L. Li, K. Shen, X.G. Lu and W.Z. Ding, *Int. J.*

Hydrogen Energy, 2010, **35**, 12191–12200.
15 S. Takenaka, Y. Orita, H. Umebayashi, H. Matsune and M. Kishida, *Appl. Catal. A,* 2008, **351**, 189–194.
16 K. Nagaoka, K. Sato, H. Nishiguchi and Y. Takita, *Appl. Catal. A,* 2007, **327**, 139–146.
17 T. Sperle, D. Chen, R. Lodeng and A. Holmen, *Appl Catal A,* 2005, **283**, 195–204.
18 F. Arena, G. Trunfio, E. Alongi, D. Branca and A. Parmaliana, *Appl Catal A,* 2004, **266**, 155–162.
19 T.S. Christensen, *Appl. Catal. A,* 1996, **138**, 285–309.
20 T. Suzuki, H.I. Iwanami, O. Iwamoto and T. Kitahara, *Int. J. Hydrogen Energy,* 2001, **26**, 935–940.
21 J. Zheng, J.J. Strohm and C.S. Song, *Fuel Process. Tech., 2008,* **89**, 440–448.
22 S. Souentie, M. Athanasiou, D.K. Niakolas, A. Katsaounis, S.G. Neophytides and C.G. Vayenas, *J. Catal.,* 2013, **306,** 116–128.
23 B. Valle, B. Aramburu, A. Remiro, J. Bilbao and A.G. Gayubo, *Appl. Catal. B,* 2014, **147**, 402–410.
24 K.O. Christensen, D. Chen, R. Lødeng and A. Holmen, *Appl. Catal. A,* 2006, **314**, 9–22.
25 J. Xu, L.W. Chen, K.F. Tana, A. Borgna and M. Saeys, *J. Catal.,* 2009, **26**, 1158–165.
26 S. Natesakhawat, R.B. Watson, X.Q. Wang and U.S. Ozkan, *J. Catal.,* 2005, **234**, 496–508.
27 J.J. Strolhm, J. Zheng and C.S. Song, *J. Catal.,* 2006, **238**, 309–320.
28 J.G. Seo, M.H. Youn and I.K. Song. *Int. J. Hydrogen Energy,* 2009, **34**, 1809–1817.
29 S.J. Han, Y. Bang, J. Yoo, J.G. Seo and I.K. Song. *Int. J. Hydrogen Energy,* 2013, **38**, 8285–8292.
30 J. Yang, X.G. Wang, L. Li, K. Shen, X.G. Lu and W.Z. Ding, *Appl. Catal. B,* 2010, **96**, 232–237.
31 A.H. Chen, T. Miyao, K. Higashiyama, H. Yamashita and M. Watanabe, *Angew. Chem. Int. Ed.,* 2010, **49**, 9895–9898.
32 N. Wang, K. Shen, L.H. Huang, X.P. Yu, W.Z. Qian and W. Chu, *ACS Catal.,* 2013, **3**, 1638–1651.
33 F. Bimbela, D. Chen, J. Ruiz, L. García and J. Arauzo, *Appl. Catal. B,* 2012, **119**, 1–12
34 L.L. Xu, H.L. Song and L.J. Chou, *Appl. Catal. B,* 2011, **108**, 177–190.
35 M.H. Amin, K. Mantri, J. Newnham, J. Tardio and S.K. Bhargava, *Appl. Catal. B,* 2012, **120**, 217–226.
36 W. Chen, G.F. Zhao, Q.S. Xue, L. Chen and Y. Lu, *Appl. Catal. B,* 2013, **137**, 260–268.
37 J. Liu, J. Yu, F.B. Su and G.W. Xu, *Catal. Sci. Technol.,* 2014, **4**, 472–481.
38 M. Wu and D.M. Hercules, *J. Phys. Chem.,* 1979, **83**, 2003–2008.
39 P. Munnik, M.E.Z. Velthoen, P.E. de Jongh, K.P. de Jong and C.J. Gommes, Angew. *Chem. Int. Ed.,* 2014, **53**, 9493–9497.
40 G.H. Li, L.J. Hu and J.M. Hill, *Appl. Catal. A,* 2006, **301**, 16–24.
41 J. Mazumder and H.I. de Lasa, *Appl. Catal. B,* 2015, **168–169**, 250–265.
42 K. Zakamura, T. Miyazawa, T. Sakurai, T. Miyao, S. Naito, N. Begum, K. Kunimori and K. Tomishige, *Appl. Catal. B,* 2008, **86**, 36–44.
43 L.P.R. Profeti, E.A. Ticianelli and E.M. Assaf, *Int. J. Hydrogen Energy,* 2009, **34**, 5049–5060.
44 X.F. Shang, X.G. Wang, W.X. Nie, X.F. Guo, X.J. Zou, W.Z. Ding and X.G. Lu, *J. Mater. Chem.,* 2012, **22**, 23806–23814.
45 M.W. Tan, X.G. Wang, X.F. Shang, X.J. Zou, X.G. Lu and W.Z. Ding, *J. Catal.,* 2014, **314**, 117–131.
46 M.W. Tan, X.G. Wang, X.X. Wang,, X.J. Zou, W.Z. Ding and X.G. Lu, *J. Catal.,* 2015, **329**, 151–166.
47 L.L Xu, H.L. Song and L.J. Chou, *Int. J. Hydrogen Energy,* 2013, **38**, 7307–7325.
48 M.P. Gonzalez-Marcos, J.I. Gutierrez-Ortiz, C. Gonzalez-Ortiz de Elguea, J.A. Delgado and J.R. Gonzalez-Velasco, *Appl. Catal. A, 1997*, **162**, 269–280.
49 P. Margineanu and A. Olariu, *J. Catal.,* 1967, **8**, 359–367.
50 Z. Boukha, C. Jiménez-González, B. de Rivas, J. R. González-Velasco, J.I. Gutiérrez-Ortiz and R. López-Fonseca, *Appl. Catal. B,* 2014, **158–159**, 190–201.
51 B.H. Yue, X.G. Wang, X.P. Ai, J. Yang, L. Li, X.G. Lu and W.Z. Ding, *Fuel Process. Technol.,* 2010, **91**, 1098–1104.
52 L.J.I. Coleman, W. Epling, R.R. Hudgins and E. Croiset, *Appl. Catal. A,* 2009, **363**, 52–63.
53 K.F. Waldner, R.M. Laine, S. Dhumrongvaraporn, S. Tayaniphan and R. Narayanan, *Chem. Mater.,* 1996, **8**, 2850–2857.
54 J.J. Guo, H. Lou, H. Zhao, D.F. Chai and X.M. Zheng, *Appl. Catal. A,* 2004, **273**, 75–82.
55 J. Zielinski, *J. Catal.,* 1982, **76**, 157–163.
56 P. Salagre, J.L.G. Fierro, F. Medina and J.E. Sueiras, *J. Mol. Catal. A,* 1996, **106**, 125–134.
57 A.M. Siouffi, *J. Chromatogr. A,* 2003, **1000**, 801–818.
58 J.B. Pang, K.Y. Qiu, Y. Wei, X.J. Lei and Z.F. Liu, *Chem. Commun.,* 2000, 477–478.
59 Y. Wei, J.G. Xu, H. Dong, J.H. Dong, K. Qiu and S.A. Jansen-Varnum, *Chem. Mater.,* 1999, **11**, 2023–2029.
60 C.D. Wagner, J.F. Moulder, L.E. Davis and W.M. Riggs, *Handbook of X-ray Photoelectron Spectroscopy*, II. Standard XPS spectra of the elements, ed. G.E. Muilenberg. Perking-Elmer Corporation, Eden Prairie, MN 1979.
61 T.L. Barr, *J. Phys. Chem.,* 1978, **82**, 1801−1810.
62 J.A. Wang, A. Morales, X. Bokhimi and O. Novaro, *Chem. Mater.,* 1999, **11**, 308**–**313.
63 M. Lo Jacono, M. Schiavello and A. Cimino, *J. Phys. Chem.,* 1971, **76**, 1044**–**1049.
64 A. Cimino, M. Lo jacono and M. Schiavello, *J. Phys. Chem.,* 1975, **79**, 243**–**249.
65 Y. Kathiraser, W. Thitsartarn, K. Sutthiumporn and S. Kawi, *J. Phys. Chem. C,* 2013, **117**, 8120**–**8130.
66 H.S. Bengaard, J.K. Nørskov, J. Sehested, B.S. Clausen, L.P. Nielsen, A.M. Molenbroek and J.R. Rostrup-Nielsen, *J. Catal.,* 2002,**209**, 365–384.
67 L.M. Aparicio, *J. Catal.,* 1997, **165**, 262−274.
68 C. Zheng, Y. Apeloig and R. Hoffmann, *J. Am. Chem. Soc.,* 1988, **110**, 749−774.

Influence of nickel content on structural and surface properties, reducibility, and catalytic behavior of mesoporous γ-alumina-supported Ni–Mg oxides for pre-reforming of liquefied petroleum gas

Graphical abstract

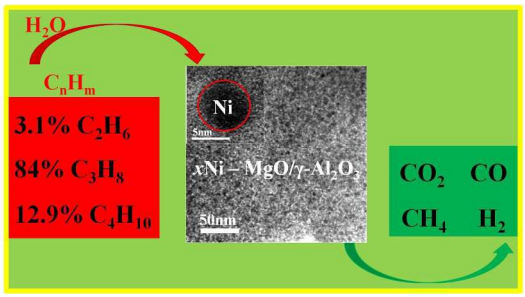

Influence of nickel content on structural and surface properties, reducibility, and catalytic properties of Ni–MgO/γ-Al_2O_3 for pre-reforming of LPG